Takemura *et al. Earth, Planets and Space* (2023) 75:20
https://doi.org/10.1186/s40623-023-01778-8

Earth, Planets and Space

FULL PAPER

Open Access

# High-frequency *S* and *S*-coda waves at ocean-bottom seismometers

Shunsuke Takemura[1*], Kentaro Emoto[2] and Lina Yamaya[3]

**Abstract**

To clarify the characteristics of high-frequency (> 1 Hz) *S* and *S*-coda waves at ocean-bottom seismometers (OBSs), we analyzed seismograms observed at permanent OBSs and inland broadband seismometers around the Kii Peninsula in southwest Japan along the Nankai Trough. The coda amplitudes (both horizontal and vertical) at the OBSs were much larger than those at the inland rock-site stations. Because coda amplitudes relative to those at inland rock-site stations have been used as site-amplification factors, large site amplifications for both components can be expected due to the presence of thick oceanic sediments just below the OBSs; however, the observed maximum *S*-wave amplitudes in the vertical component exhibited similar attenuation trends against epicentral distances at both OBS and inland stations. To clarify the causes of this discrepancy, we conducted numerical simulations of seismic wave propagation using various three-dimensional seismic velocity structure models. The results demonstrated that coda waves at OBSs mostly comprise multiple scattered waves within a thick (> 2 km) sedimentary layer; consequently, coda amplitudes at OBSs become much larger than those at inland rock-site stations. Our numerical simulations also confirmed the generation of large coda amplitudes at regions with seawater depths $\geq$ 4 km, where no OBS was deployed. However, the thick sedimentary layer and seawater have limited effects on maximum *S*-wave amplitudes at the OBSs. Given that the effects of a thick sedimentary layer and seawater on *S* and *S*-coda waves differ, we concluded that the coda-normalization technique for site-amplification correction against a rock-site station could not be applied if stations are located within regions above the thick sedimentary layer or deeper sea depths. The site amplifications at the OBSs were corrected according to the horizontal-to-vertical ratios at each OBS; we adjusted the simulated horizontal envelopes at the OBSs using these ratios of the observed *S*-coda waves. As well as inland seismometers, the site-corrected simulation results practically reproduced the observed high-frequency envelopes at OBSs.

**Keywords** Ocean-bottom seismometer, Seismic wave scattering, Coda wave, Site amplification, Ground motion simulation

*Correspondence:
Shunsuke Takemura
shunsuke@eri.u-tokyo.ac.jp
Full list of author information is available at the end of the article

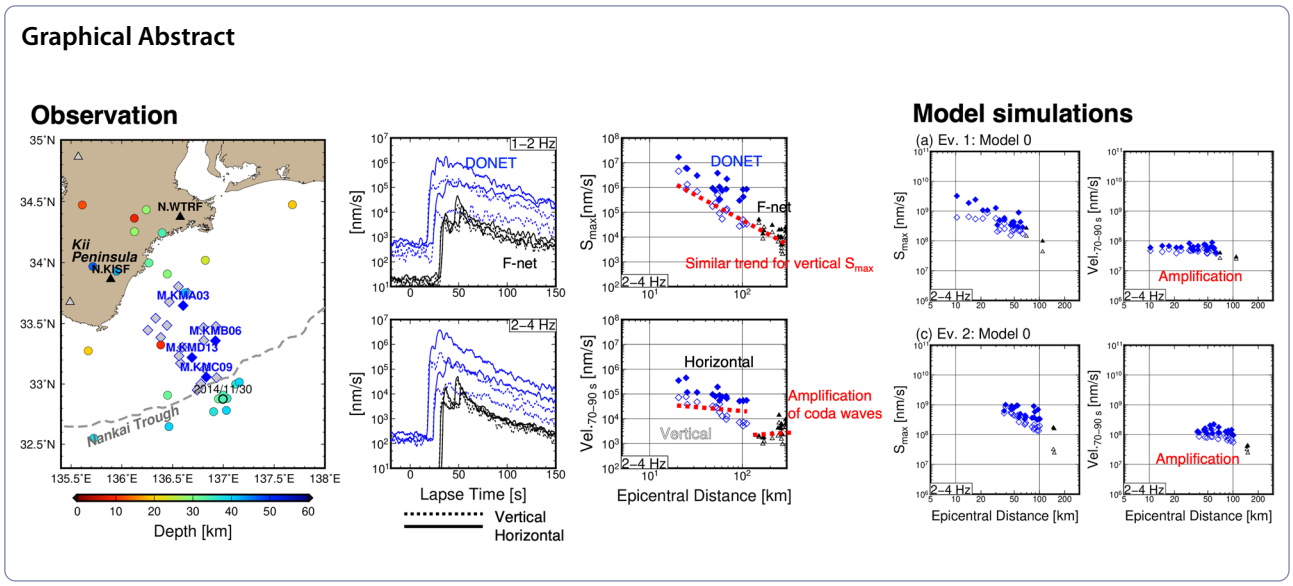


## Introduction

Recent developments in offshore observations provide great opportunities to investigate not only structural heterogeneities (including both path and site effects) but also various seismic phenomena in offshore regions. To reveal the characteristics of megathrust zones, campaign observations, such as the Cascadia Initiative (e.g., Toomey et al. 2014) and the HOBITSS experiment (e.g., Wallace et al. 2016b), have been conducted worldwide. Extensive campaign observations for geophysical surveys and aftershock observations have been also conducted in Japan (e.g., Shinohara et al. 2005; Fujie et al. 2018). Recently, permanent ocean-bottom seismometer (OBS) networks (Dense Oceanfloor Network for Earthquakes and Tsunamis (DONET) and Seafloor Observation Network for Earthquakes and Tsunamis along the Japan Trench) were deployed by the Japan Agency for Marine–Earth Science and Technology (JAMSTEC) and the National Research Institute for Earth Science and Disaster Resilience (NIED), respectively (Aoi et al. 2020). Implementing both permanent and campaign offshore observations has allowed the detection of weak seismic signals associated with offshore seismic phenomena (e.g., Yamashita et al. 2015; Todd et al. 2018; Nishikawa et al. 2019; Plata-Martinez et al. 2021), estimations of shallower heterogeneous structures(e.g., Ruan et al. 2014, 2018; Tonegawa et al. 2017; Yamaya et al. 2021), and evaluation of site amplifications (e.g., Kubo et al. 2018; Gomberg 2018).

To obtain a better understanding of seismic phenomena at OBSs, the characteristics of seismic wave propagation through offshore regions should be investigated. The effects of heterogeneous structures in offshore regions, such as seawater and oceanic sediments, on low-frequency (< 0.5 Hz) surface waves have been well documented (e.g., Shapiro et al. 1998; Noguchi et al. 2016; Volk et al. 2017; Kaneko et al. 2019); however, their effects on high-frequency (> 1 Hz) *S* and *S*-coda waves have not been studied. High-frequency seismic waves enable the investigation of not only the characteristics of shallow and small seismic events (e.g., Yabe et al. 2019, 2021; Yamaya et al. 2022) and shallower high-resolution structural heterogeneities (e.g., Kamei et al. 2012; Davy et al. 2021), but also seawater-temperature monitoring based on teleseismic *T* waves (e.g., Wu et al. 2020). Figure 1b, c shows examples of high-frequency seismic waves observed at the DONET and Full Range Seismograph Network of Japan (F-net) stations during an earthquake that occurred at 08:00 on November 30, 2011 (Japan Standard Time; JST) near the Nankai Trough (Fig. 1a). F-net is a full-range seismograph network with sensors installed at outcrop rock sites. Thus, F-net stations are widely used as reference sites for correcting and estimating site amplifications against rock sites (e.g., Takemoto et al. 2012; Kubo et al. 2018; Yabe et al. 2019, 2021). The amplitudes of *S*-wave coda at the DONET stations were much larger than those at the F-net stations (Fig. 1b and the bottom panel of Figs. 1c). Additionally, at the DONET stations, the horizontal coda amplitudes (blue filled diamonds) were much larger than those of the vertical component (blue open diamonds).

*S*-coda waves are constructed by superposition of scattered waves from randomly distributed scatterers within the lithosphere (e.g., Aki 1969; Aki and Chouet 1975). Owing to the superposition of randomly

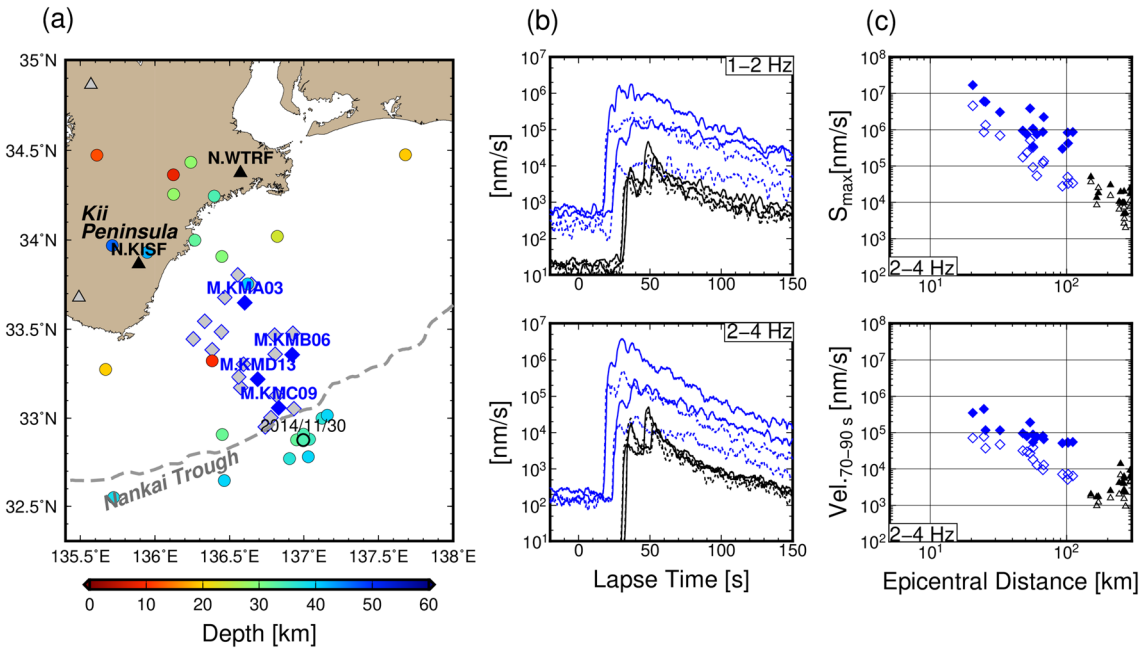


**Fig. 1** Map and examples of observed seismogram envelopes around the Nankai Trough. The colored circles in **a** represent local earthquakes used in this study, and the triangles and diamonds are locations of F-net and DONET stations, respectively (Aoi et al. 2020). Filled triangles and diamonds are stations used in **b**. The solid and dotted lines in **b** are horizontal and vertical envelopes. The envelopes at DONET and F-net stations are represented by blue and black lines, respectively. **c** $S_{max}$ and coda amplitudes as a function of epicentral distance. The filled blue and open diamonds are horizontal and vertical amplitudes at DONET stations, respectively. The filled and open triangles are those at F-net stations

scattered waves, path effects at later coda parts are considered as common at all stations. Additionally, the effects of the source radiation pattern are expected to be large for *S* waves at near-source stations even for higher (> 2 Hz) frequencies but weak for later coda portions (e.g., Sato et al. 1997; Takemura et al. 2016; Trugman et al. 2021). Thus, the relative amplitudes of coda amplitudes at a certain reference station are mainly dependent on the source energy and the local site beneath a certain seismic station. According to the coda envelopes (Fig. 1b) and coda amplitudes (Fig. 1c, bottom panel), $S_{max}$ for both horizontal and vertical components at the DONET stations is expected to be amplified against those at the F-net stations. In this study, we defined "site amplification" as relative amplitudes against rock-site stations, such as F-net stations. In addition, for modeling seismic energies of small events, such as small earthquakes and tremors, attenuation curves and site correction against a rock site for maximum *S*-wave amplitudes have been widely used (e.g., Yabe et al. 2019, 2021; Wech 2021). Thus, we focused on maximum amplitudes as a function of epicentral distance. In Fig. 1c (upper panel), however, the maximum *S*-wave ($S_{max}$) amplitudes in the vertical component obeyed a similar attenuation trend as a function of epicentral distance for both DONET and F-net stations. One-odder fluctuations of maximum amplitudes could be explained by the source radiation pattern and seismic wave scattering (e.g., Hoshiba 2000; Yoshimoto et al. 2015; Takemura et al. 2016). This implies that vertical $S_{max}$ amplitudes at DONET stations might not be significantly amplified, although coda amplitudes were obviously larger than those at F-net stations. The amplifications of horizontal $S_{max}$ at DONET stations from the attenuation trend of horizontal $S_{max}$ at F-net stations were confirmed.

The coda-normalization method for estimating and correcting site amplifications has been widely used in inland regions worldwide (e.g., Phillips and Aki 1986; Yoshimoto et al. 1993; Takemoto et al. 2012). The observations in Fig. 1 suggest that the characteristics of *S* and *S*-coda waves in offshore regions differ significantly from those of typical inland regions. In this study, to understand the characteristics of high-frequency seismic wave propagation in offshore regions, we investigated observed *S*-wave and *S*-coda amplitudes from local earthquakes around the Nankai Trough (Fig. 1a). To evaluate the effects of offshore heterogeneities, we conducted numerical simulations of high-frequency seismic wave propagation in various-type heterogeneous models. Combined analysis of both observed and simulated seismograms revealed differences in the

characteristics of high-frequency $S$ and $S$-coda waves between offshore and inland seismic stations.

### Data and method: observed data

We used seismograms of DONET strong motion and F-net broadband velocity records from local earthquakes. Our target region was southeast off the Kii Peninsula located in the Nankai subduction zone, Japan. Intraslab-regular and interplate slow earthquakes often occur in this region (e.g., Nakano et al. 2015; Takemura et al. 2020a, 2022). We selected local regular earthquakes with $M \geq 3.5$ from the unified hypocenter catalog of the Japan Meteorological Agency (JMA). These earthquakes occurred during the observation period of DONETs (Fig. 1a and Additional file 1: Table S1). To focus our attention on the effects of structural heterogeneities on high-frequency seismic waves, we did not use slow earthquakes, because their signals are weak, and their moment rate functions are complicated (e.g., Yabe et al. 2019; Takemura et al. 2022) as compared with regular earthquakes.

We applied a band-pass filter at various frequency ranges (0.5–1.0, 0.75–1.5, 1.0–2.0, 1.5–3.0, 2.0–4.0, and 3.0–6.0 Hz) to the observed velocity seismograms. The envelopes of the filtered seismograms were synthesized using the Hilbert transformation. The horizontal envelopes were obtained by calculating the root-mean-square (RMS) vector sum of the X- and Y-component (EW- and NS-component) envelopes. The horizontal and vertical envelopes were smoothed by taking the 3-s moving average. Using these envelopes at the DONET and F-net stations, we evaluated the $S_{max}$ for each frequency band. The coda amplitudes were calculated by averaging the amplitudes at lapse times of 70–90 s. The resultant envelopes and amplitudes for each earthquake are shown in Additional file 1: Figs. S2–S51.

### Data and method: numerical simulations

We conducted numerical simulations of seismic wave propagation using a local three-dimensional (3D) model. The 3D seismic velocity structure model in our simulations was the same as that described by Takemura

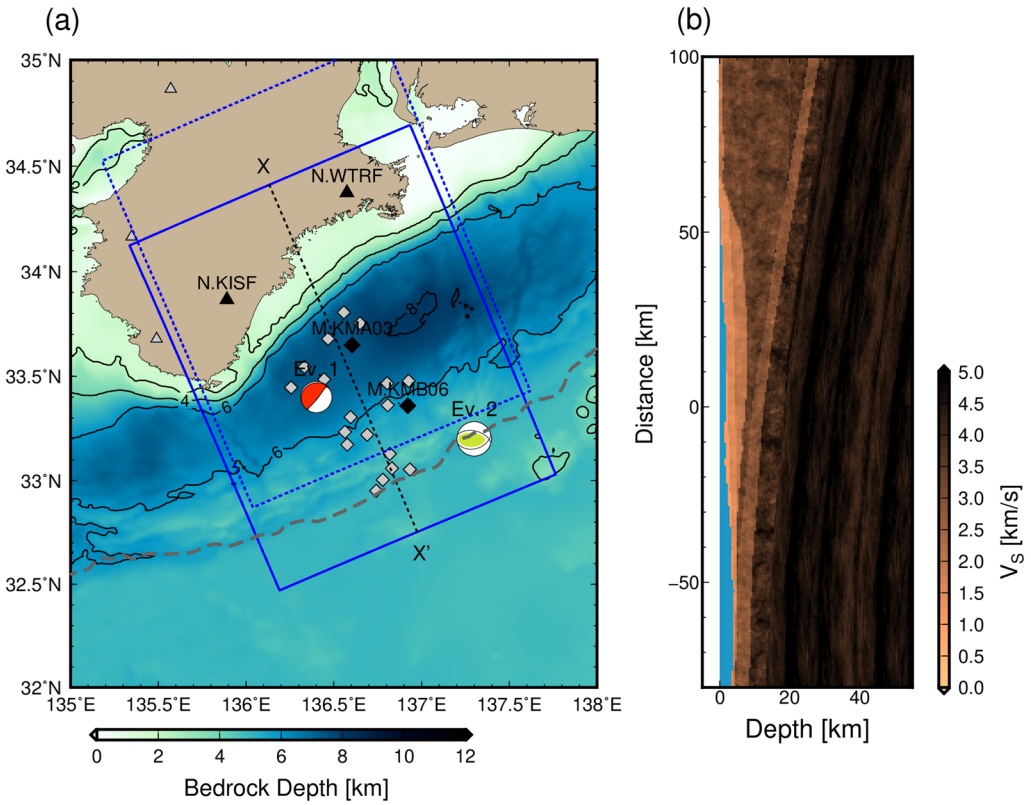


**Fig. 2** Map view and cross-section of our simulation model. The blue solid rectangle in **a** is the horizontal coverage of our simulation model for Fig. 7–Fig. 12. The blue dotted rectangle is also the horizontal coverage of the simulation model but for Figure S1 only. Plotted focal mechanisms of Events 1 and 2 were the source models used in this study. The colors in focal spheres of Events 1 and 2 are representing focal depths same as in Fig. 1a. The background color and contour lines represent the bedrock depths of Koketsu et al. (2012). The gray, bold, dashed line in **a** is the deformation front (Nankai Trough). The cross-section of $S$-wave velocity structure along the X-X′ profile in **a** is shown in **b**. The X-axis is the X direction in **a**

et al. (2020b); that is, the model was constructed by combining Koketsu et al. (2012) and Tonegawa et al. (2017). The model by Koketsu et al. (2012) includes the bedrock topography, crust, and oceanic crust, and mantle of the subducting Philippine Sea Plate. The bedrock depths increased around the DONET stations (Fig. 2a). The 3D sedimentary structure in the offshore region was constructed by interpolation and extrapolation of the one-dimensional (1D) *S*-wave velocity structure beneath the DONET stations (Tonegawa et al. 2017). The detailed physical parameters of each layer are presented in Table 1 (Takemura et al. 2020b). The minimum *S*-wave velocity within the elastic volume was 1.0 km/s. We employed ETOPO1 (Amante and Eakins 2009) as the bathymetric model. The model also includes seawater and air columns. The *P*- and *S*-wave velocities and density in the seawater layer were 1.5 km/s, 0.0 km/s, and 1.04 g/cm$^3$, respectively. The air column was modeled as a vacuum condition with *P*- and *S*-wave velocities of 0.0 km and a density of 0.001 g/cm$^3$. This layered structure model reproduces not only long-period ground motions (e.g., Takemura et al. 2018, 2019), but also the envelope shapes of high-frequency (>1 Hz) seismic waves (Takemura et al. 2020b).

Small-scale velocity fluctuations, which enhance the scattering of high-frequency seismic waves (summarized in Sato et al. 2012), were modeled by embedding random velocity fluctuations, which were constructed using an exponential autocorrelation function (e.g., Klimeš 2002; Sato et al. 2012). The correlation lengths and RMS values within the oceanic mantle and others (Table 1) were obtained from previous studies (Furumura and Kennett 2005; Takemura et al. 2017). Small-scale velocity fluctuations within the sedimentary layer have limited effects on direct-*S* waves (Iwaki et al. 2018; Takemura et al. 2020b); however, to enhance coda waves, we assumed the presence of small-scale velocity fluctuations within the sedimentary layer. Because this model is the reference model in the later discussions, we referred to this heterogeneous model as "Model 0".

**Table 1** Parameters of small-scale velocity fluctuations in each layer

| Layer | ACF-type | Correlation length | RMS value |
|---|---|---|---|
| Air and sea water | – | – | – |
| Sediment layers | Exponential | Isotropic: 1 km | 0.03 |
| Crust | Exponential | Isotropic: 1 km | 0.03 |
| Mantle | – | – | – |
| Oceanic crust | Exponential | Isotropic: 1 km | 0.03 |
| Oceanic mantle | Exponential | Horizontal: 20 km Vertical: 1 km | 0.03 |

ACF: autocorrelation function

We used Open-Source Seismic Wave Propagation Code (OpenSWPC) (Maeda et al. 2017) based on the staggered grid finite-difference method. The model covered a volume of $200 \times 160 \times 62.5$ km$^3$ (Fig. 2a, blue rectangle), which was discretized by a uniform grid interval of 0.025 km. The cross-section of the *S*-wave velocity structure of Model 0 along profile X'–X is shown in Fig. 2b. Because the minimum S-wave velocity in the solid column is 1 km/s, as mentioned above, our simulations with a 0.025-km grid discretization can evaluate seismic wave propagation for frequencies up to approximately 6 Hz. Such large-scale simulations were conducted using the Earth Simulator at JAMSTEC. Each simulation for preparing 150-s seismograms by 150,000 timesteps required 32 TB of computer memory and 4.4 h of computation time using 2000 vector elements (cores) of the Earth Simulator.

We synthesized seismograms for Events 1 and 2 (Fig. 2a, focal spheres). Event 1 was an interplate earthquake that occurred at 11:39 on April 1, 2016 (JST). To model the seismic waves from an intraslab earthquake, we selected Event 2, which occurred at 08:29 on September 7, 2004 (JST). The focal mechanisms and locations of these events were fixed as parameters from the centroid moment tensor solutions in Takemura et al. (2020a) (Table 2). To focus our attention on the effects of structural heterogeneities, we employed a 0.1-s Küpper wavelet as a source time function.

To discuss the effects of various-type heterogeneities on high-frequency seismic wave propagation, we prepared three additional heterogeneous models: a model without sedimentary layers (Model 1), a model without a seawater layer (Model 2), and a model without both seawater and sedimentary layers (Model 3). In Model 1, the physical parameters of the sedimentary layers were replaced by those within the basement. In Model 2, the physical parameters of the seawater layer were replaced with those of the air. In Model 3, the physical parameters of both the sedimentary and seawater layer were replaced with those of the basement and the air, respectively. Recent studies

**Table 2** Source parameters of Events 1 and 2

| | Lon. [°E] | Lat. [°N] | Dep. [km] | $m_{rr}$ | $m_{\theta\theta}$ | $m_{\phi\phi}$ | $m_{r\theta}$ | $m_{r\phi}$ | $m_{\theta\phi}$ | Exp. |
|---|---|---|---|---|---|---|---|---|---|---|
| Ev. 1 | 136.4 | 33.4 | 10.0 | 3.786 | − 1.407 | − 0.624 | 5.760 | 7.431 | − 1.554 | 24 |
| Ev. 2 | 137.3 | 33.2 | 24.0 | 4.326 | − 11.195 | − 0.4324 | − 1.413 | 1.400 | − 6.731 | 25 |

demonstrated significant effects of later phases due to thick oceanic sediments and seawater on receiver function imaging (e.g., Akuhara and Mochizuki 2015; Kim et al. 2021). In the present study, we did not discuss the effects of bathymetry. The previous studies numerically revealed that the topographic scattering of seismic waves effectively generates early coda waves just after maximum *S* wave amplitudes but can be expected to be limited effects on direct-*S* and later coda waves (e.g., Imperatori and Mai 2015; Takemura et al. 2015, 2017, 2020b).

The F-net N.KISF station, which was used as a reference, was located near the model boundary in our simulations. To assess the stability of the simulated coda envelopes at this station, we conducted a simulation of Event 1 using the model region (Fig. 2a, dashed blue rectangle). Additional file 1: Fig. S1 shows comparisons of the horizontal envelopes at the N.KISF station between the model regions (Fig. 2a, blue solid and dashed rectangles). The phases of small-scale random fluctuations differ in the models because we used the same random fluctuations data, but a certain specific numerical grid represents the different locations in the two models. Thus, the resultant envelopes are not identical. However, the envelope shape and temporal decay characteristics of the coda showed almost similar trends, and the differences are within the fluctuation range. Thus, we believe that simulation-region selection may have limited effects on our results. Hereafter, we discuss high-frequency *S* and *S*-coda waves at the F-net N.KISF and DONET stations using the simulation results in the model (Fig. 2a, blue solid rectangle).

#### Results: observed seismograms

The characteristics of high-frequency *S* and *S*-coda waves confirmed in Fig. 1b, c were also observed in other earthquakes (Additional file 1: Figs. S2–S51). Although envelope shapes at DONET stations were various due to source locations and the heterogeneous 3D model, DONET coda amplitudes for both horizontal and vertical components are larger than those at F-net stations. In our data set (Fig. 1a and Additional file 1: Table S1), more than ten intraplate earthquakes near the Trough axis exist. Vertical coda amplitudes of such earthquakes at KMA- and KME-nodes were smaller than others (as shown in the bottom panel of Fig. 1c). We recognized that coda signals for frequency ranges 0.5–1.0 Hz and 0.75–1.5 Hz could be available in only a few moderate ($M_{JMA} > 4$) earthquakes. Therefore, we focused our attention on the characteristics of seismic wave propagation at frequencies > 1 Hz. The coda amplitudes of the horizontal and vertical components at the DONET stations were larger than those at the F-net stations; however, the vertical $S_{\max}$ amplitudes at both DONET and F-net stations obeyed similar attenuation characteristics. DONET stations were deployed just above the thick sedimentary layers (Fig. 2a). The characteristic differences between *S* and *S*-coda waves within sedimentary basins were first described by Idei et al. (1985), who pointed out that the amplification characteristics of *S* and *S*-coda waves may be different if the seismic station is located within a thick sedimentary basin. Additionally, we confirmed a similar possibility at DONET stations, where thick (> 2 km) oceanic sediments exist (e.g., Kamei et al. 2012; Tonegawa et al. 2017).

Figure 3 shows the relationship between hypocenter depths and relative coda amplitudes at four DONET stations (KMA03, KMB06, KMC09, and KMD13) normalized against those at N.KISF (the station locations are shown in Fig. 1a). In the coda-normalization method, these values are considered as the site-amplification factors of *S* waves. An earthquake that occurred at 11:39 on April 1, 2016 (JST), was located at a depth of 28 km in the JMA catalog; however, this earthquake was an interplate earthquake at a depth of approximately 10 km (e.g., Wallace et al. 2016a; Takemura et al. 2020a). Therefore, we modified the depth of the earthquake to 10 km (Additional file 1: Table S1). Because the oceanic Moho of the Philippine Sea plate in this region exists at depths of 10–15 km, other earthquakes are intraslab earthquakes occurred within the oceanic mantle. The relative coda amplitudes of intraslab earthquakes increased with increasing hypocenter depth. This tendency appeared to be due to the effects of depth-difference in coda generation from intraslab earthquakes rather than local site effects.

We calculated horizontal-to-vertical (H/V) ratio envelopes and discarded envelopes with coda-to-noise ratios less than 5. Figure 4 shows the H/V ratio envelopes at M.KMB06 for available earthquakes. Owing to the differences in earthquake locations and source radiation patterns, the H/V ratios at lapse times of 20–40 s (body wave parts) exhibited temporal variations with larger fluctuations of each event. The H/V ratios were almost constant at lapse times ≥ 70 s, despite the variance in epicenter locations and earthquake depths (Fig. 1a). Figure 5 shows the map of the coda H/V ratios for frequency ranges of 1–2 Hz and 2–4 Hz. The coda H/V ratios were calculated using the average H/V ratios at lapse times of 70–90 s. The coda H/V ratios at F-net stations were almost 1. We compared estimated coda H/V ratios at DONET stations with horizontal site amplifications estimated by Yabe et al. (2019). Yabe et al. (2019) estimated site amplifications at DONET stations using distance attenuation curves of $S_{\max}$ from regular earthquakes in this region. Although estimated site amplification factors varied due to estimation methods

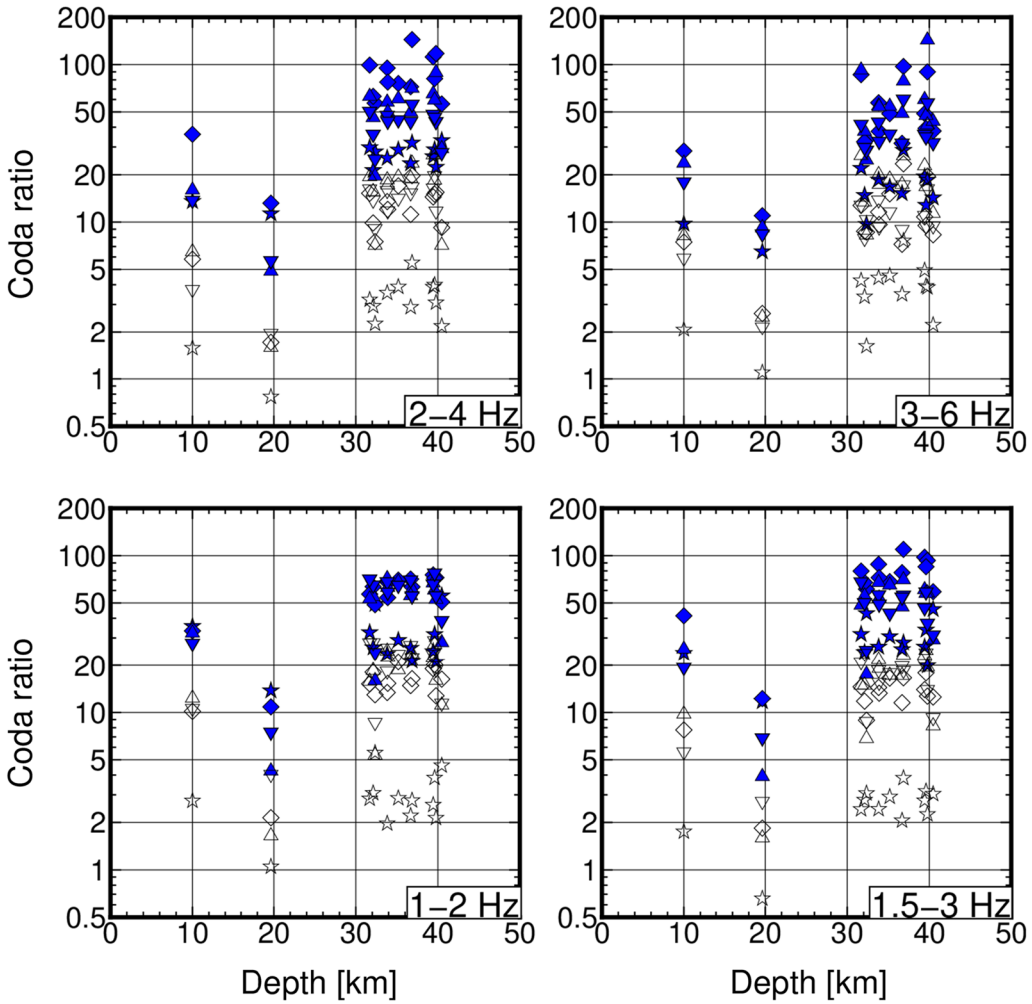


**Fig. 3** Coda amplitude ratios at DONET stations as a function of hypocenter depth. The stars, diamonds, triangles, and inverse triangles are coda-amplitude ratios at M.KMA03, M.KMB06, M.KMC09, and M.KMD13, respectively. The filled and open symbols represent coda amplitude ratios for the horizontal and vertical components, respectively

(e.g., Kubo et al. 2020), these values correspond well with the horizontal site amplifications estimated by Yabe et al. (2019), except for M.KMC10 and M.KMC11.

The H/V ratio has been widely used for site-amplification and shallower structure estimations at inland strong motion stations (e.g., Lermo and Chávez-García 1993; Field and Jacob 1995; Konno and Ohmachi 1998; Kawase et al. 2018). Recently, Dhakal et al. (2017) investigated H/V ratios of *S* waves to discuss nonlinear site effects at OBSs around Sagami Bay, Japan. We tried to correct the horizontal $S_{max}$ amplitudes at the DONET stations using the average coda H/V ratio at each station. Figure 6 shows the relationships between the $S_{max}$ amplitudes and epicentral distances for an earthquake that occurred at 08:00 on 30 November 2014 (JST). Both the vertical and corrected horizontal $S_{max}$ amplitudes at the DONET stations obeyed similar attenuation characteristics. This result indicated that as well as inland seismometers, the H/V ratios for the coda part were practically able to correct site amplifications for horizontal ground motions at OBSs. This possibility will be numerically validated in a later section.

#### Results: simulations of seismic wave propagation

Numerical simulations of seismic wave propagation within various heterogeneous models help us understand the observed characteristics of high-frequency *S* and *S*-coda waves. As mentioned above, we assumed the uniform *S*-wave velocity of the sedimentary layer of 1 km/s to simplify the discussions on the effects of heterogeneities on high-frequency seismic wave propagation. In this section, thus, we focused our attention on observed characteristics of both $S_{max}$ and coda amplitudes at both DONET and F-net stations.

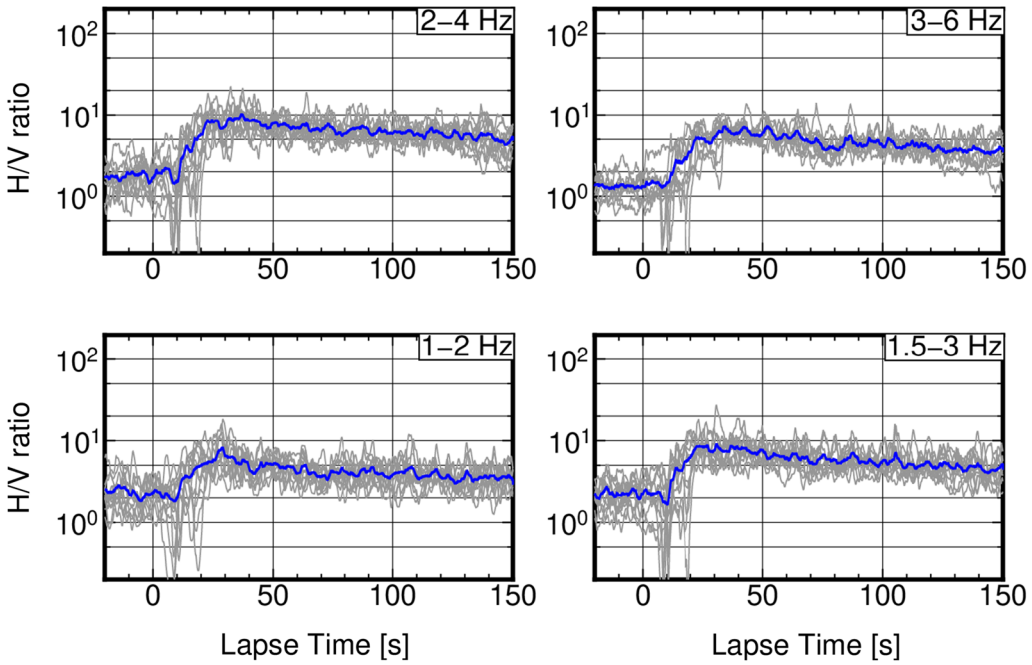


**Fig. 4** H/V ratio envelopes at M.KMB06. The gray lines are H/V ratio envelopes for each earthquake. Signal-to-noise ratios for coda parts of each envelopes are larger than 5. The blue envelopes are stacked H/V ratio envelopes for each frequency band

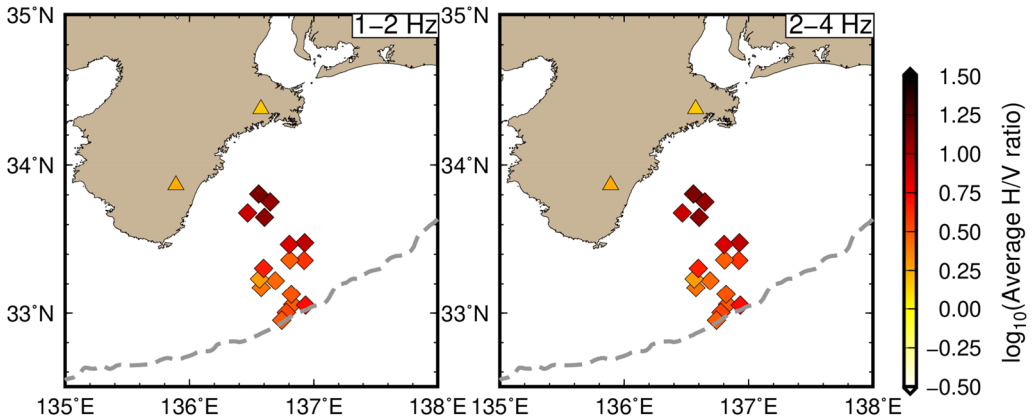


**Fig. 5** Spatial variations of stacked H/V ratios of coda waves for different frequency ranges (1.0–2.0 and 2.0–4.0 Hz)

Figure 7 shows the simulated envelopes for Events 1 and 2 at stations N.KISF and M.KMB06. The amplitudes of the coda waves at M.KMB06 (blue lines) around lapse times of 60–100 s were larger than those at N.KISF (black lines). The differences between N.KISF and M.KMB06 coda amplitudes for Event 2 are larger than those for Event 1. Although the observed horizontal coda amplitudes at the DONET stations were much larger than those in the vertical component (Fig. 1b and Additional file 1), the simulated horizontal (solid lines) and vertical (dashed lines) coda amplitudes did not differ significantly.

The effects of thick sedimentary and seawater layers on *S* and *S*-coda waves are presented in Fig. 8, which shows the simulated horizontal envelopes at M.KMB06 and N.KISF for the additional three heterogeneous models (Models 1–3). The coda amplitudes of Model 1 (Fig. 8a) were smaller than those of Model 0. Additionally, the effects of the thick sedimentary layer appeared at N.KISF, because N.KISF is located close to the coastline. The influence of the thick, low-velocity sedimentary layer at

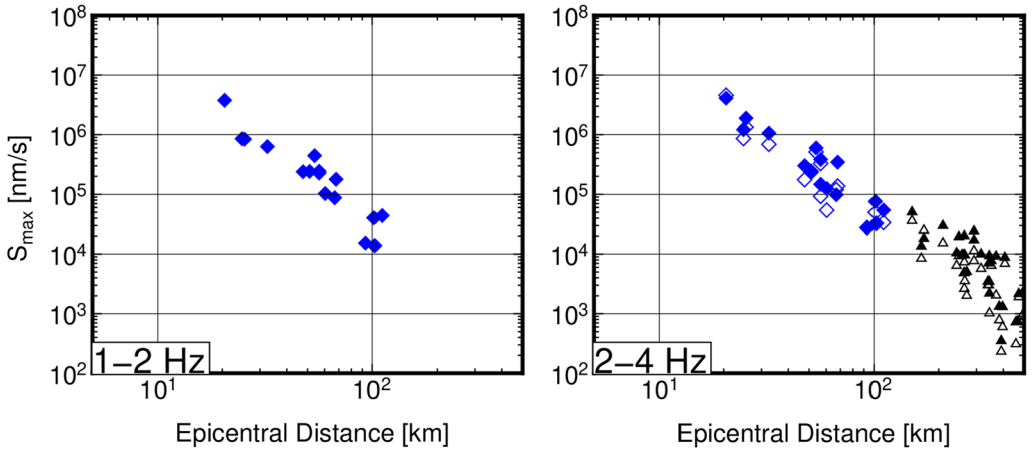


**Fig. 6** Attenuation characteristics of the $S_{max}$ amplitude after correction using H/V ratios. The filled blue and open diamonds are horizontal and vertical amplitudes at DONET stations, respectively. The filled and open triangles are those at F-net stations

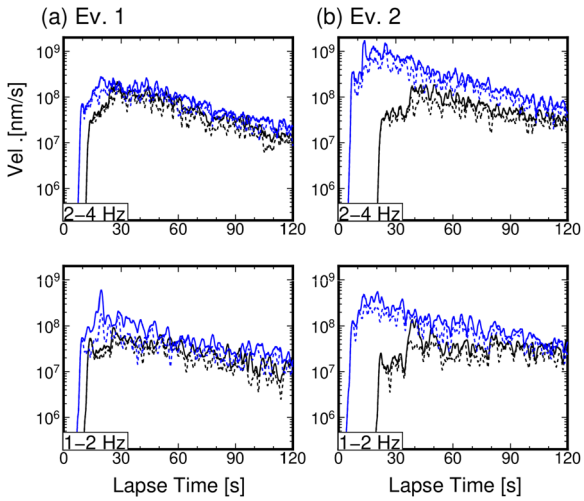


**Fig. 7** Simulated horizontal (solid lines) and vertical (dotted lines) envelopes for frequency ranges of 1.0–2.0 Hz and 2.0–4.0 Hz for Model 0. The envelopes for **a** Event 1 and **b** Event 2. The blue and black lines denote envelopes at M.KMB06 and N.KISF stations, respectively

M.KMB06 appeared to be stronger than that at N.KISF. Owing to the lack of a seawater layer (Model 2; Fig. 8b), the coda amplitude at M.KMB06 became slightly smaller than those in Model 0. Based on these comparisons, we confirmed that thick, low-velocity sediments had the strongest effect on *S*-coda amplitudes. However, the $S_{max}$ amplitudes of each heterogeneous model did not drastically change relative to those of Model 0.

Figure 9 shows the simulated $S_{max}$ and *S*-coda amplitudes at 2–4 Hz for different models (Models 0 and 3). We also plotted the simulated $S_{max}$ and *S*-coda amplitudes at other frequency bands (1–2 and 3–6 Hz) for Model 0 to discuss frequency-dependent features of $S_{max}$ and *S*-coda amplitudes (Additional file 1: Fig. S52). A few F-net stations were included in our simulation region. Thus, we also evaluated amplitudes at virtual inland stations with an interval of 0.05°. The characteristics of simulated vertical $S_{max}$ and *S*-coda amplitudes (Fig. 9 and Additional file 1: Fig. S52) were in good agreement with the observations (Fig. 1c and Additional file 1: Fig. S2–S51). The simulated $S_{max}$ at the DONET and inland (Figs. 9a, c, and Additional file 1: Fig. S52, blue diamonds and triangles, respectively) stations exhibited a similar attenuation trend against epicentral distance, even for Model 0. Although *S*-coda amplitudes in Model 3 (Fig. 9b and d) were almost the same irrespective of epicentral distance, coda amplitudes at DONET stations in Model 0 (except for one or two DONET stations) were larger than those at inland stations (Fig. 9a, c, and S52). The frequency-dependent characteristics of differences in the *S*-coda amplitudes of Model 0 between the F-net and DONET stations were not clearly observed (Fig. 9a, c, and Additional file 1: Fig. S52). We found slightly smaller coda amplitudes at distances around 100 km for Event 2 (intraplate earthquake; Fig. 9c). This feature vanished by replacing the physical parameters within the sedimentary layer with those within the basement (Fig. 9d).

Figure 10 (top panels) shows the spatial distributions of the horizontal coda amplitudes for Event 1 at the F-net, DONET, and virtual seismic stations at an interval of 0.05°. Moreover, we plotted the thickness of the Japan Integrated Velocity Structure Model (JIVSM) sedimentary layer and confirmed that areas with large coda amplitudes corresponded well to areas with thick (> 2 km) sedimentary layers. Furthermore, the coda amplitudes for sediments > 2-km-thick were

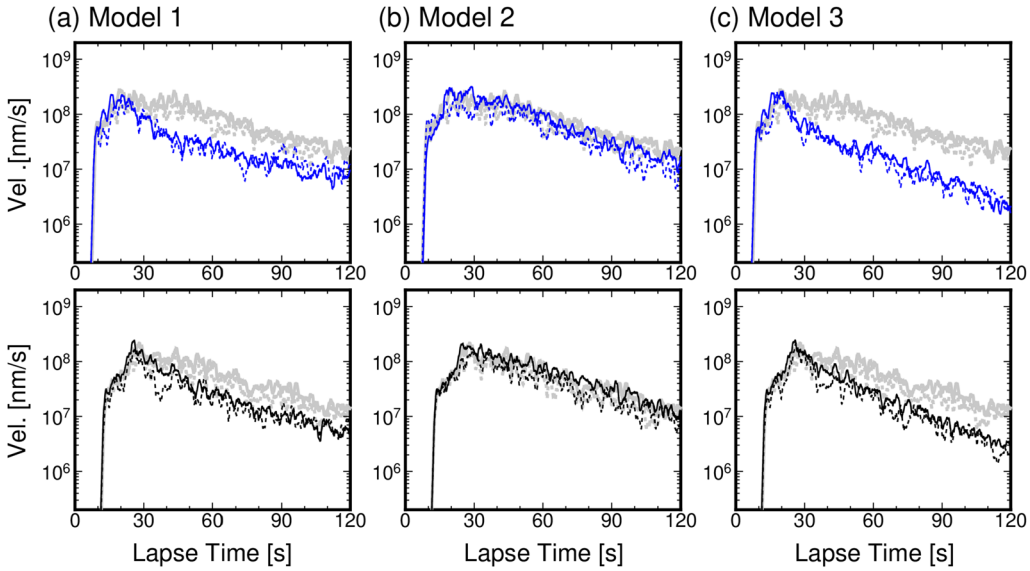


**Fig. 8** Simulated envelopes of Event 1 for **a** Model 1, **b** Model 2, and **c** Model 3 at M.KMB06 (upper) and N.KISF (bottom). The horizontal and vertical envelopes are illustrated by solid and dotted lines, respectively. The background gray envelopes are simulation results of Model 0

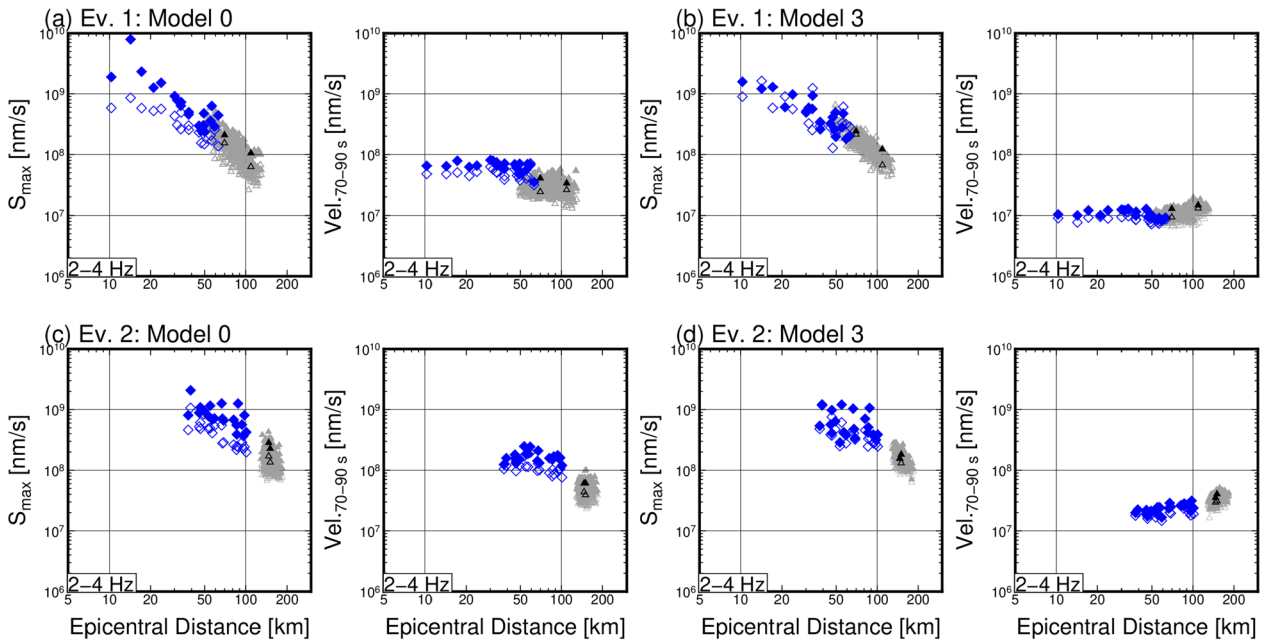


**Fig. 9** $S_{max}$ and coda amplitudes for the frequency range 2.0–4.0 Hz as a function of epicentral distance. Plotted simulated amplitudes of Event 1 for **a** Model 0 and **b** Model 3 and of Event 2 for **c** Model 0 and **d** Model 3. The filled blue and open diamonds are horizontal and vertical amplitudes at DONET stations, respectively. The filled and open triangles are those at inland F-net stations. To increase the data of inland stations, we also evaluated simulated amplitudes at inland virtual seismic stations at an interval of 0.05° (gray triangles)

almost constant (Fig. 10, bottom panels). This suggested that the energies of the coda waves were trapped and homogenized within the thick sedimentary layers.

We confirmed that large coda amplitudes appeared in the outer-rise region (Fig. 10, top panels). In the outer-rise region, the sedimentary layer is not so thick (< 2 km), but sea depths are greater than 4 km (Fig. 10, bottom panels). Additional file 1: Fig. S53 shows the simulated envelopes at a virtual station (137.05°E, 32.80°N) in the outer-rise region. We confirmed that the

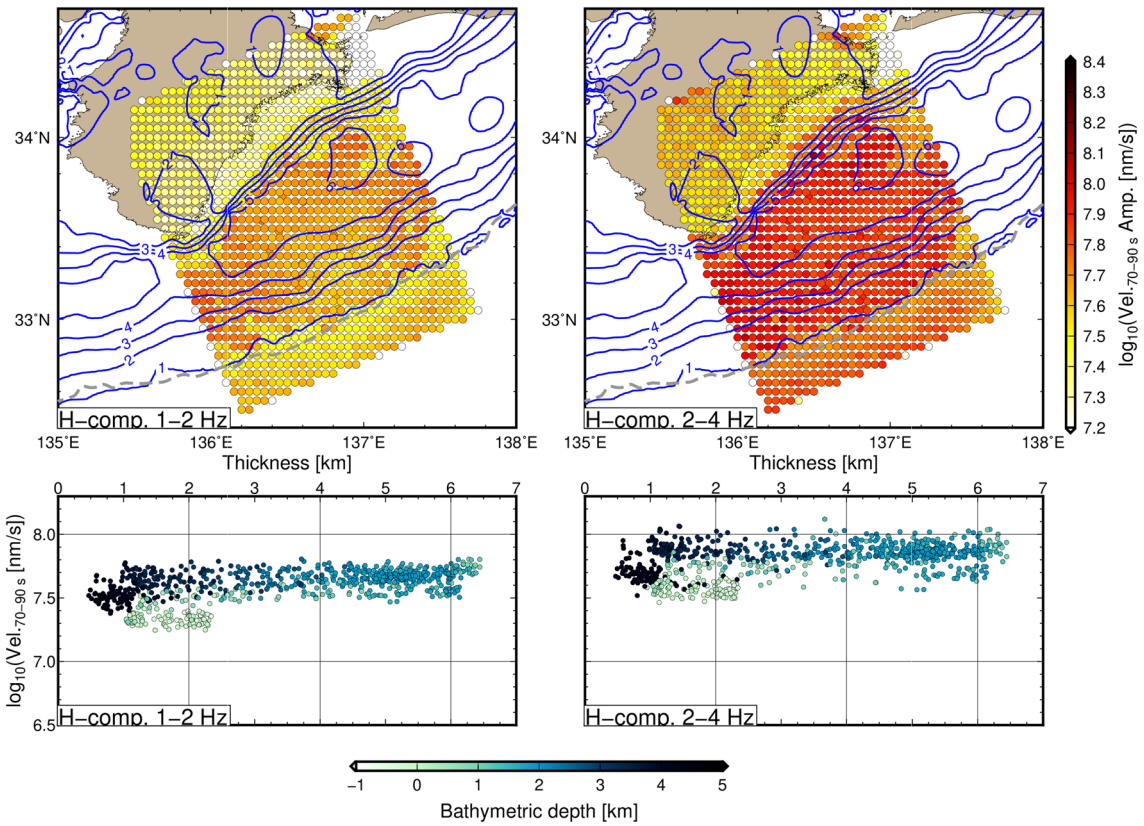


**Fig. 10** Spatial variations of simulated coda amplitudes for Event 1. Coda amplitudes were evaluated by calculating the average of amplitudes at lapse times of 70 s–90 s. The upper panels are the map view plots of horizontal coda amplitudes for frequency ranges 1.o–2 Hz and 2.0–4.0 Hz. The blue contour lines are the thickness of the JIVSM sedimentary layer. The bottom panels show the horizontal coda amplitudes as a function of sediment thickness. The colors in circles of the bottom panels represent the bathymetric depths

seawater layer influenced coda amplitudes at a station located in the outer-rise region, although the effects of the seawater layer were limited in regains with a thick sedimentary layer (see Fig. 8). Unfortunately, because no observation station is deployed in the outer-rise region, we could not compare the characteristics of simulated envelopes with observations.

To discuss how seismic waves scatter at later coda parts, we then calculated the energy fluxes at M.KMB06 for the simulations of Event 1 for each model. Using the stress ($\tau$) and velocity ($v$) wavefields, we obtained the energy flux of the $j$th component ($j = x, y, z$), $e_j$, by $-\sum_k \tau_{jk} v_k$. We evaluated the propagation directions of coda waves using energy flux vectors. Figure 11 shows the histograms of the propagation directions for coda waves at lapse times of 70–90 s in each model. We used a simulated time series of the velocity and stress fields at M.KMB06 from the simulation results of Event 1. The angle $\theta$ was measured from the z-axis, and $\theta = 0$ indicated downward propagation. Angle $\phi$ represents the horizontal azimuth measured from the $X$-axis, which is the same as that in Fig. 2a. The horizontal azimuth, $\phi$, was uniformly distributed irrespective of the heterogeneous models. This indicated that scattered waves were randomly incident from the scatterers to the M.KMB06 station. In Model 3 (typical crust), the angle $\theta$ tended to be concentrated around 60° to 120°, indicating that scattered waves propagated horizontally from far scatterers. However, in the heterogeneous models, except for Model 3, angle $\theta$ was not localized around 60°–120°. This suggested that scattering within the sedimentary layer and/or multiple reflections between the bedrock and sea surface generates vertically propagating $S$-waves, which causes the amplification and elongation of coda waves.

According to the observed seismograms and simulations in various-type heterogeneous models, we found that coda waves at DONET stations mostly comprise a superposition of scattered or reflected waves within a thick (> 2 km) sedimentary layer. Low-velocity sedimentary basin was developed in 100-km scale along both strike and dip directions (Figs. 2a and 11). Once $S$ waves radiated from a seismic source incident within thick low-velocity sediments, $S$-wave energy is trapped

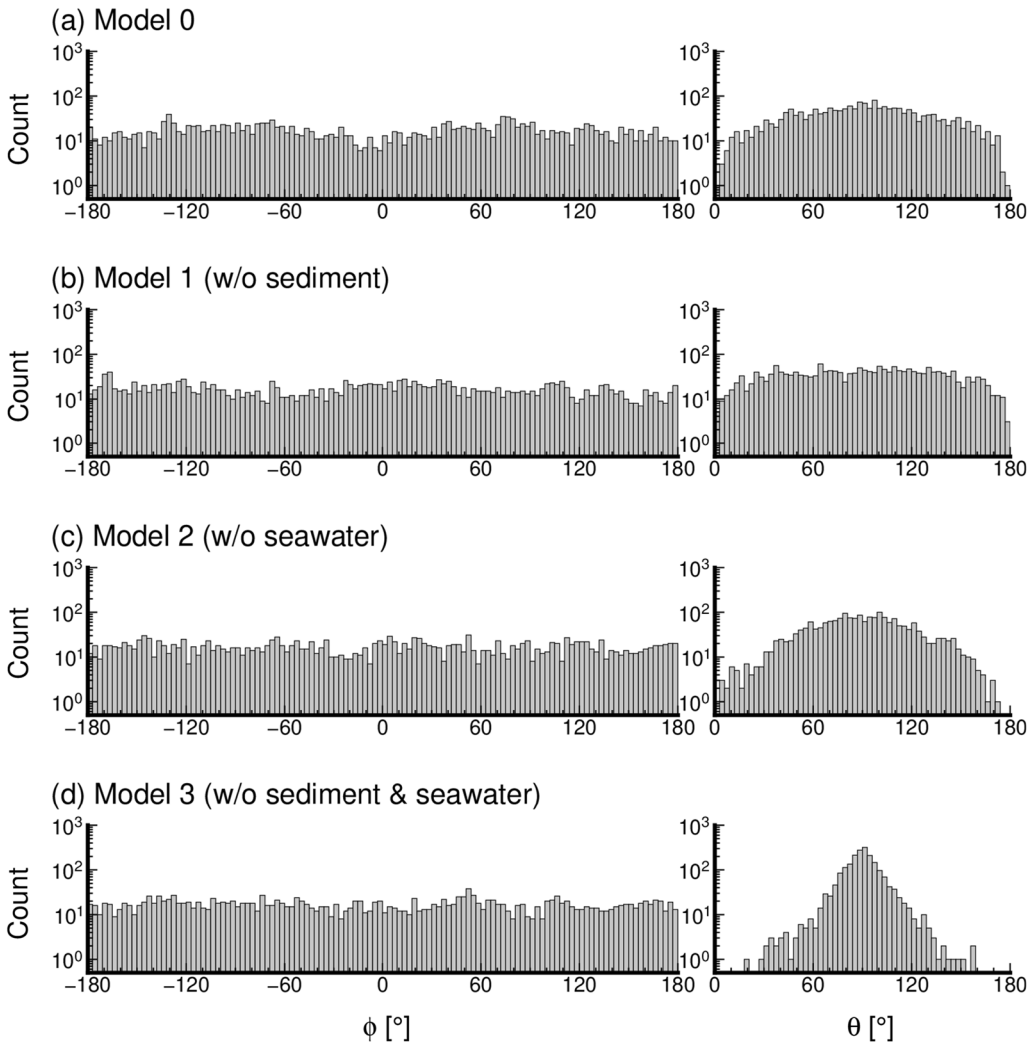


**Fig. 11** Distributions of directions of energy flux for coda waves in various types of heterogeneous models. The angle $\theta$ is measured from the *Z*-axis, and $\theta = 0$ means a downward propagation. The angle $\varphi$ *i*s the horizontal azimuth measured from the X-axis. The X-axis is similar to that described in Fig. 2a

within the sediments; consequently, coda waves at DONET stations mostly comprise multiple scattered waves within the sediments. By contrast, direct *S* waves propagated through the sediments just beneath the stations only once. Thus, the amplification characteristics of high-frequency *S* and *S*-coda waves due to thick low-velocity sediments are completely different.

Large-scale thick sedimentary structures also exist in various inland regions (e.g., the Kanto, Osaka, Niigata, Los Angeles, Seattle, and Mexico Basins). Additionally, thick oceanic sediments exist in other subduction zones (Straume et al. 2019), such as the Japan Trench (Takagi et al. 2020; Yamaya et al. 2021), Hikurangi margin (Eberhart-Phillips and Bannister 2015; Kaneko et al. 2019), and Cascadia (Ruan et al. 2014; Gomberg 2018). In such regions, as Idei et al. (1985) first pointed out, the coda-excitation mechanism can differ from that in a typical lithosphere. Moreover, we found that the seawater layer also affected the coda at OBSs; however, the impact was limited in the regions with thick (> 2 km) sedimentary layer. The coda-normalization method for estimating or correcting site amplifications ageist a rock-site station cannot be applied to stations within thick sediments and seawater.

### A realistic simulation for the 2016 southeast off Mie earthquake

In this section, we compared our simulation result with the observation of an interplate earthquake on 1

April 2016. To directly compare the simulations with the observed strong motions, our simulation result was adjusted by estimated coda H/V ratios at DONET stations. This direct comparison between observed and simulated strong ground motion provided us the opportunity for discussion of practical ground motion simulation, including site amplification effects.

We conducted a finer-scale simulations of the seismic wave propagation for Event 1 in a model region that covered an area discretized by a finer grid (0.015 km) (Fig. 12a, blue rectangle). We employed the same 3D model and source model of Event 1 as in previous simulations but the minimum *S*-wave velocity is 0.5 km/s, which allowed evaluation of seismic wave propagation for frequencies less than 4.7 Hz. We conducted simulations of the model using five realizations of small-scale random velocity fluctuations. The simulated envelopes for each frequency band were then calculated by stacking the envelopes of the five random realizations. Each simulation for preparing 75-s seismograms by 150,000 timesteps required 50 TB of computer memory and 6.1 h of computation time using 2736 vector elements (available full vector elements) of the Earth Simulator.

Owing to our limited knowledge of small-scale heterogeneities, it is difficult to obtain a realistic moment rate function that includes high-frequency (>1 Hz) components. Thus, after simulations using a 0.1-s Küpper source wavelet, the simulated envelopes for each frequency band were adjusted by ratios between the simulated and observed horizontal $S_{max}$ amplitudes at N.KISF. Additionally, the horizontal envelopes at DONET stations were multiplied by the observed coda H/V ratios at the corresponding stations (Fig. 5). Because the simulation region was narrowed because of the finer spatial grids for a minimum *S*-wave velocity of 0.5 km/s, F-net stations were consequently located close to the model boundaries (Fig. 13a). Thus, in our new simulations, we focused on the $S_{max}$ amplitudes at the F-net and DONET stations and envelope shapes at the DONET stations.

Figure 12b shows a comparison of the $S_{max}$ amplitudes between the simulations and observations. We discarded the data of the M.KME node (4 northwestern DONET stations just above the source of Event 1) because of strong nonlinear site responses during this event (Kubo et al. 2019). The adjusted simulation results reproduced the observed $S_{max}$ amplitudes of both horizontal and vertical component. Figure 13 shows examples of comparisons between the observed and simulated envelopes for the frequency range 2.0–4 Hz. Although we assumed an unrealistic 0.1-s Küpper pulse, the envelope shapes at the DOENT stations were characterized by spindle shapes. This significant pulse broadening was also

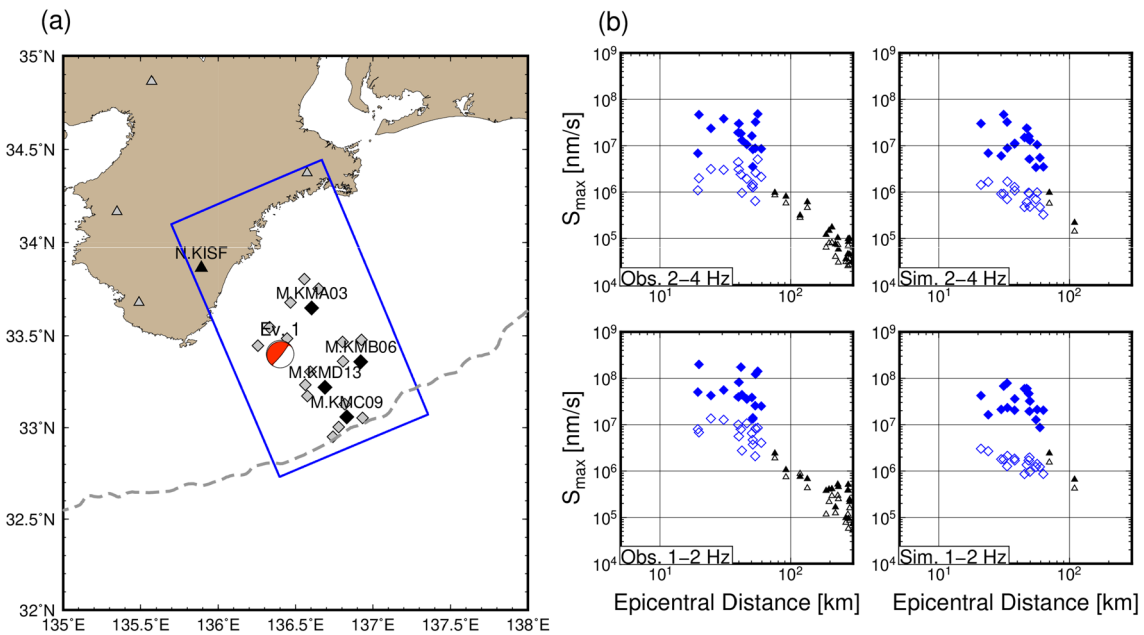


**Fig. 12** **a** Map of simulation settings and **b** comparisons between simulated and observed amplitudes for frequency ranges of 1.0–2.0 Hz and 2.0–4.0 Hz. The blue solid rectangle and red focal mechanism in **a** are the model region and assumed source model, respectively. **b** Plots of the $S_{max}$ amplitudes at the DONET and F-net stations. The filled blue and open diamonds are horizontal and vertical amplitudes at DONET stations, respectively. The filled and open triangles are those at F-net stations

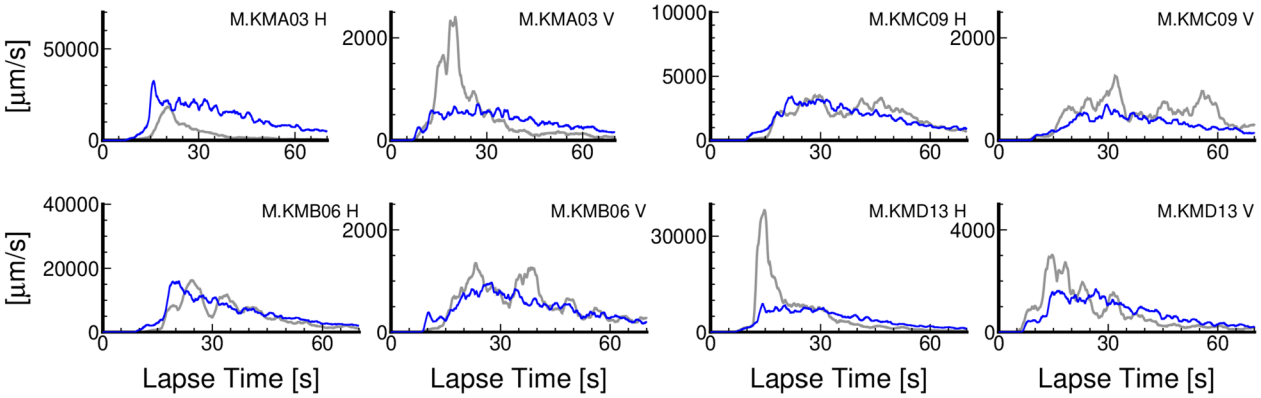


**Fig. 13** Comparisons of observed and simulated envelopes for the frequency range of 2.0–4.0 Hz. Gray and blue lines represent observed and simulated envelopes, respectively. Station locations are given in Fig. 11a. The simulation results were normalized by the horizontal $S_{max}$ amplitude at N.KISF

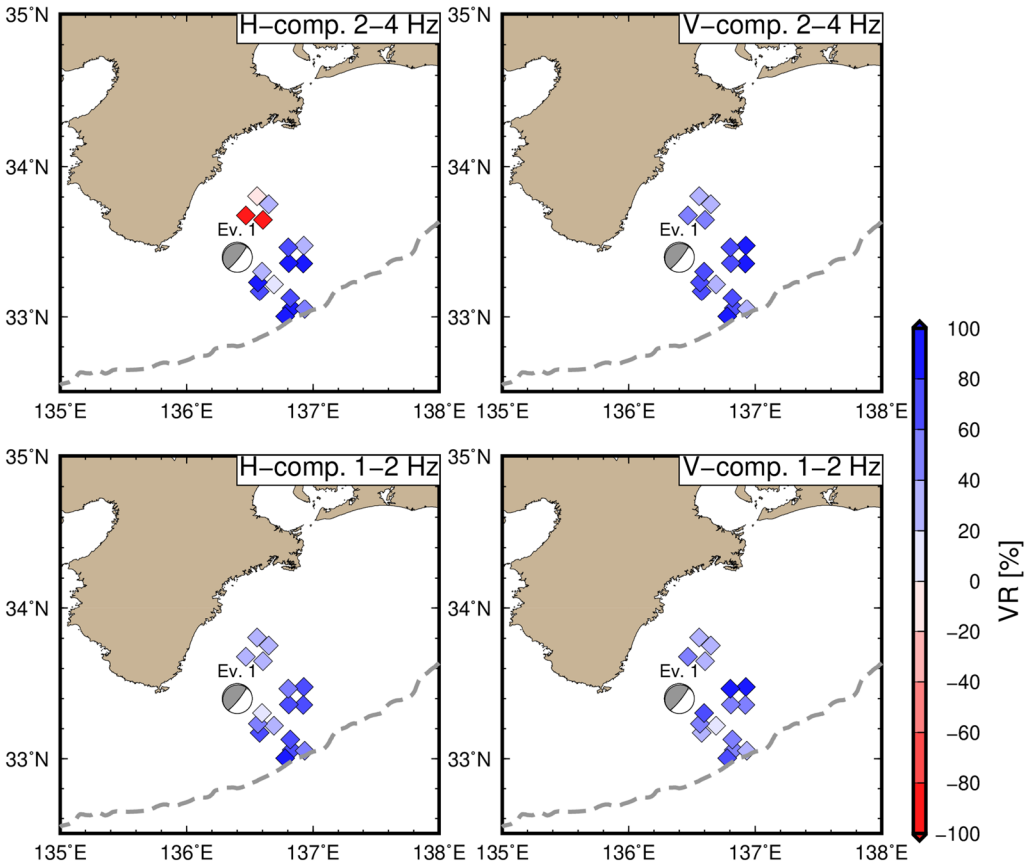


**Fig. 14** Spatial variations in VRs between observed and simulated envelopes. The simulation results were normalized by the horizontal $S_{max}$ amplitude for each frequency band at N.KISF

caused by thick oceanic sediments beneath the stations (Takemura et al. 2020b).

To illustrate the reproducibility of our simulations in terms of amplitudes and envelope shapes, Fig. 14 shows the variance reductions (VRs) between the observed and simulated envelopes. The VRs of $j$-component ($j$ = horizontal or vertical) at $i$th station were evaluated as follows:

$$VR_{ij} = \left[1 - \frac{\int_0^T \left(v_{ij}^{obs}(t) - v_{ij}^{syn}(t)\right)^2 dt}{\int_0^T \left(v_{ij}^{obs}(t)\right)^2 dt}\right],$$

where $v^{obs}(t)$ and $v^{syn}(t)$ were observed and simulated envelopes, and the length of time window ($T$) is 75 s. Although detailed parameters for the source time function and random small-scale heterogeneity within oceanic sediments are not well known, this simulation reproduced the characteristics of seismogram envelopes at the DONET stations, suggesting that the described simulation model and method for adjusting site amplification based on coda H/V ratios worked well. The stations at the KMA node (4 northeastern stations) exhibited low VRs, and the simulation using a point source model could not reproduce envelopes in directions close to the null axis of the Event 1 focal mechanism. The $10.6 \times 3.4$-km$^2$ rectangle fault of this earthquake reproduced tsunami records at DONET stations (e.g., Wallace et al. 2016a; Kubota et al. 2018); therefore, a complicated rupture process for generating high-frequency seismic energy is expected on the fault of this earthquake. By introducing detailed source rupture heterogeneities, the discrepancies between the observed and simulated envelopes will be improved in future studies.

## Conclusions

Using observed and simulated seismograms, we investigated the characteristics of high-frequency $S$ and $S$-coda waves at the OBSs around the Nankai Trough. High-frequency coda waves at OBSs mostly comprise multiple scattered waves within a thick (>2 km) sedimentary layer beneath OBSs. Although seismic waves of coda parts at DONET stations were trapped and scattered within the whole sediment, direct $S$ waves propagated through the sediments just beneath the stations only once. This suggests that the amplification characteristics of high-frequency $S$ and $S$-coda waves due to thick low-velocity sediments are completely different. Although we could not directly compare our simulations with observations, large coda amplitudes also appeared in the outer-rise region, where the sea depths are deeper than approximately 4 km. Thus, the coda-normalization technique for estimating or adjusting site amplification against a rock-site station cannot be applied at stations within thick sediments and seawater, which are not only OBSs but also stations within large inland sedimentary basins.

The observed horizontal coda amplitudes at the OBSs are much larger than those of the vertical component, which is caused by site amplifications due to thin, lower (<0.5 km/s) velocity structures just beneath the stations. We adjusted the simulated horizontal envelopes using the observed H/V ratio of the coda waves, resulting in the adjusted simulation results practically reproducing the observed high-frequency envelopes of the OBSs. These findings demonstrated that the H/V ratios of the coda waves worked well for correcting the site amplifications.

### Abbreviations

| | |
|---|---|
| 1D | One-dimensional |
| 3D | Three-dimensional |
| DONET | Dense Oceanfloor Network for Earthquakes and Tsunamis |
| ERI-JURP | Earthquake Research Institute, the University of Tokyo Joint Usage/Research Program |
| F-net | Full-range seismograph network |
| HOBITSS | Hikurangi Ocean Bottom Investigation of Tremor and Slow Slip |
| H/V | Horizontal-to-vertical |
| JAMSTEC | Japan Agency for Marine-Earth Science and Technology |
| JIVSM | Japan Integrated Velocity Structure Model |
| JST | Japan Standard Time |
| NIED | National Research Institute for Earth Science and Disaster Resilience |
| OpenSWPC | Open-Source Seismic Wave Propagation Code |
| VR | Variance reduction |

## Supplementary Information

The online version contains supplementary material available at https://doi.org/10.1186/s40623-023-01778-8.

**Additional file 1: Figure S1.** shows simulated horizontal envelopes at N.KISF using morel regions from Figure 2. **Figures S2-S51** observed envelopes, maximum amplitudes, and coda amplitudes for all used earthquakes. The source parameters of Figure S2–S51 are listed in Table S1. **Figure S52** shows simulated maximum S and coda wave amplitudes for 1–2 and 3–6 Hz. Model settings are the same as in Figure 9. **Figure S53** is simulated envelopes at a virtual outer-rise station (137.05ºE, 32.80ºN) for Models 1–3.

### Acknowledgements

Numerical simulations of seismic wave propagation were conducted using the Earth Simulator on JAMSTEC and Wisteria/BDEC-01 at the Information Technology Center, University of Tokyo. We thank Suguru YABE, Hisahiko KUBO, Satoru BABA, Tatsuhiko SAITO, Katsuhiko SHIOMI, and Kazuo YOSHIMOTO for their helpful discussions. We would like to thank Editage (www.editage.com) for help with English language editing. We also acknowledge an anonymous reviewer, Dr. S. Padhy, the editor Prof. Y. Wang and the editor-in-chief Prof. T. Sagiya for careful reviewing and constructive comments, which helped to improve the manuscript.

### Author contributions

ST conducted waveform analysis and numerical simulations and drafted the manuscript; KE performed theoretical considerations of coda generation; and

ST, KE, and LY interpreted the observed characteristics of high-frequency *S* and *S*-coda waves. All the authors read and approved the final manuscript.

**Funding**
This study was supported by a JSPS KAKENHI Grant (No. JP21K03696) and a Grant-in-Aid for Scientific Research on Transformative Research Areas "Science of Slow-to-Fast earthquakes" (Grant Nos. JP21H05200 and JP21H05205). This study was also supported by ERI JURP 2021-S-B102.

**Availability of data and materials**
We used HinetPy (https://doi.org/10.5281/zenodo.3695076) to download DONET and F-net data from the National Research Institute for Earth Science and Disaster Resilience (2019a, b; https://hinetwww11.bosai.go.jp/auth/?LANG=en). We used OpenSWPC (v.5.0.2; https://doi.org/10.5281/zenodo.3712650) and a local 3D model (Koketsu et al. 2012) from https://www.jishin.go.jp/evaluation/seismic_hazard_map/lpshm/12_choshuki_dat/. The 1D *S*-wave velocity structures beneath the DONET stations are available at https://doi.org/10.5281/zenodo.4158946. Figure images were drawn using Generic Mapping Tools (Wessel et al. 2013), and the Seismic Analysis Code (Goldstein and Snoke 2005; Helffrich et al. 2013) was used for part of the signal processing. The centroid moment tensor solutions of Takemura et al. (2020a) are available at https://doi.org/10.5281/zenodo.3674161. The simulation data used in this study are available from the corresponding author upon request.

## Declarations

**Ethics approval and consent to participate**
Not applicable.

**Consent for publication**
Not applicable.

**Competing interests**
The authors declare that they have no competing interests.

**Author details**
[1]Earthquake Research Institute, The University of Tokyo, 1-1-1 Yayoi, Bunkyo-ku, Tokyo 113-0032, Japan. [2]Institute of Seismology and Volcanology, Faculty of Science, Kyushu University, 744 Motooka, Nishi, Fukuoka, Japan. [3]Network Center for Earthquake, Tsunami and Volcano, National Research Institute for Earth Science and Disaster Resilience, 3-1 Tennodai, Tsukuba, Ibaraki 305-0006, Japan.

Received: 19 May 2022 Accepted: 24 January 2023
Published online: 06 February 2023

**References**

Aki K (1969) Analysis of the seismic coda of local earthquakes as scattered waves. J Geophys Res 74:615–631. https://doi.org/10.1029/JB074i002p00615

Aki K, Chouet B (1975) Origin of coda waves: source, attenuation, and scattering effects. J Geophys Res 80:3322–3342. https://doi.org/10.1029/JB080i023p03322

Akuhara T, Mochizuki K (2015) Hydrous state of the subducting Philippine sea plate inferred from receiver function image using onshore and offshore data. J Geophys Res Solid Earth 120:8461–8477. https://doi.org/10.1002/2015JB012336

Amante C, Eakins BW (2009) ETOPO1 1 arc-minute global relief model: Precedures, data sources and analysis. NOAA Technical Memorandum NESDIS NGDC-24. NOAA Technical Memorandum NESDIS NGDC-24 National Geophysical Data Center, NOAA 19. https://doi.org/10.7289/V5C8276M

Aoi S, Asano Y, Kunugi T et al (2020) MOWLAS: NIED observation network for earthquake, tsunami and volcano. Earth, Planets and Space. https://doi.org/10.1186/s40623-020-01250-x

Davy RG, Frahm L, Bell R et al (2021) Generating high-fidelity reflection images directly from full-waveform inversion: Hikurangi subduction zone case study. Geophys Res Lett. https://doi.org/10.1029/2021GL094981

Dhakal YP, Aoi S, Kunugi T et al (2017) Assessment of nonlinear site response at ocean bottom seismograph sites based on S-wave horizontal-to-vertical spectral ratios: a study at the Sagami bay area K-NET sites in Japan. Earth, Planets and Space 69:29. https://doi.org/10.1186/s40623-017-0615-5

Eberhart-Phillips D, Bannister S (2015) 3-D imaging of the northern Hikurangi subduction zone, New Zealand: variations in subducted sediment, slab fluids and slow slip. Geophys J Int 201:838–855. https://doi.org/10.1093/gji/ggv057

Field E, Jacob K (1995) A comparison and test of various site-response estimation techniques, including three that are not reference-site dependent. Bull Seismol Soc Am 85:1127–1143. https://doi.org/10.1785/BSSA0850041127

Fujie G, Kodaira S, Kaiho Y et al (2018) Controlling factor of incoming plate hydration at the north-western Pacific margin. Nat Commun 9:3844. https://doi.org/10.1038/s41467-018-06320-z

Furumura T, Kennett BLN (2005) Subduction zone guided waves and the heterogeneity structure of the subducted plate: Intensity anomalies in northern Japan. J Geophys Res 110:B10302. https://doi.org/10.1029/2004JB003486

Goldstein P, Snoke A (2005) SAC Availability for the IRIS Community. In: Incorporated Institutions for Seismology Data Management Center Electronic Newsletter. https://ds.iris.edu/ds/newsletter/vol7/no1/193/sac-availability-for-the-iris-community/

Gomberg J (2018) Cascadia onshore-offshore site response, submarine sediment mobilization, and earthquake recurrence. J Geophys Res Solid Earth 123:1381–1404. https://doi.org/10.1002/2017JB014985

Helffrich G, Wookey J, Bastow I (2013) The seismic analysis code. Cambridge University Press, Cambridge

Hoshiba M (2000) Large fluctuation of wave amplitude produced by small fluctuation of velocity structure. Phys Earth Planet Inter 120:201–217. https://doi.org/10.1016/S0031-9201(99)00165-X

Idei T, Horike M, Iwata T (1985) Seismic coda waves observed on a sedimentary basin. Zisin 38:217–232. https://doi.org/10.4294/zisin1948.38.2_217

Imperatori W, Mai PM (2015) The role of topography and lateral velocity heterogeneities on near-source scattering and ground-motion variability. Geophys J Int 202:2163–2181. https://doi.org/10.1093/gji/ggv281

Iwaki A, Maeda T, Morikawa N et al (2018) Effects of random 3D upper crustal heterogeneity on long-period ($\geq$ 1 s) ground-motion simulations. Earth, Planets and Space 70:156. https://doi.org/10.1186/s40623-018-0930-5

Kamei R, Pratt RG, Tsuji T (2012) Waveform tomography imaging of a megasplay fault system in the seismogenic Nankai subduction zone. Earth Planet Sci Lett 317–318:343–353. https://doi.org/10.1016/j.epsl.2011.10.042

Kaneko Y, Ito Y, Chow B et al (2019) Ultra-long duration of seismic ground motion arising from a thick, low-velocity sedimentary wedge. J Geophys Res Solid Earth 124:10347–10359. https://doi.org/10.1029/2019JB017795

Kawase H, Mori Y, Nagashima F (2018) Difference of horizontal-to-vertical spectral ratios of observed earthquakes and microtremors and its application to S-wave velocity inversion based on the diffuse field concept. Earth, Planets and Space 70:1. https://doi.org/10.1186/s40623-017-0766-4

Kim H, Kawakatsu H, Akuhara T et al (2021) Receiver function imaging of the amphibious ne japan subduction zone—effects of low-velocity sediment layer. J Geophys Res Solid Earth. https://doi.org/10.1029/2021JB021918

Klimeš L (2002) Correlation functions of random media. Pure Appl Geophys 159:1811–1831. https://doi.org/10.1007/s00024-002-8710-2

Koketsu K, Miyake H, Suzuki H (2012) Japan Integrated Velocity Structure Model Version 1. Proceedings of the 15th World Conference on Earthquake Engineering 1–4

Konno K, Ohmachi T (1998) Ground-motion characteristics estimated from spectral ratio between horizontal and vertical components of microtremor. Bull Seismol Soc Am 88:228–241. https://doi.org/10.1785/BSSA0880010228

Kubo H, Nakamura T, Suzuki W et al (2018) Site Amplification characteristics at Nankai seafloor observation network DONET1, Japan, evaluated using spectral inversion. Bull Seismol Soc Am. https://doi.org/10.1785/0120170254

Kubo H, Nakamura T, Suzuki W et al (2019) Ground-motion characteristics and nonlinear soil response observed by DONET1 seafloor observation network during the 2016 southeast off-mie, Japan, earthquake. Bull Seismol Soc Am 109:976–986. https://doi.org/10.1785/0120170296

Kubo H, Nakamura T, Suzuki W, et al (2020) Site characteristics of DONET1 seafloor observation network, Japan, evaluated by HVRS of coda and ambient noise. In: Proceedings of the 17th World Conference on Earthquake Engineering. Sendai, Japan

Kubota T, Suzuki W, Nakamura T et al (2018) Tsunami source inversion using time-derivative waveform of offshore pressure records to reduce effects of non-tsunami components. Geophys J Int 215:1200–1214. https://doi.org/10.1093/GJI/GGY345

Lermo J, Chávez-García FJ (1993) Site effect evaluation using spectral ratios with only one station. Bull Seismol Soc Am 83:1574–1594. https://doi.org/10.1785/BSSA0830051574

Maeda T, Takemura S, Furumura T (2017) OpenSWPC: an open-source integrated parallel simulation code for modeling seismic wave propagation in 3D heterogeneous viscoelastic media 4. Seismology. Earth, Planets and Space. https://doi.org/10.1186/s40623-017-0687-2

Nakano M, Nakamura T, Kaneda Y (2015) Hypocenters in the Nankai trough determined by using data from both ocean-bottom and land seismic networks and a 3D velocity structure model: Implications for seismotectonic activity. Bull Seismol Soc Am 105:1594–1605. https://doi.org/10.1785/0120140309

National Research Institute for Earth Science and Disaster Resilience (2019a) NIED DONET. In: National Research Institute for Earth Science and Disaster Resilience

National Research Institute for Earth Science and Disaster Resilience (2019b) NIED F-net. In: National Research Institute for Earth Science and Disaster Resilience. https://doi.org/10.17598/NIED.0005

Nishikawa T, Matsuzawa T, Ohta K et al (2019) The slow earthquake spectrum in the Japan trench illuminated by the S-net seafloor observatories. Science 365:808–813. https://doi.org/10.1126/science.aax5618

Noguchi S, Maeda T, Furumura T (2016) Ocean-influenced Rayleigh waves from outer-rise earthquakes and their effects on durations of long-period ground motion. Geophys J Int 205:1099–1107. https://doi.org/10.1093/gji/ggw074

Phillips WS, Aki K (1986) Site amplification of coda waves from local earthquakes in central California. Bull Seismol Soc Am 76:627–648. https://doi.org/10.1785/BSSA0760030627

Plata-Martinez R, Ide S, Shinohara M et al (2021) Shallow slow earthquakes to decipher future catastrophic earthquakes in the Guerrero seismic gap. Nat Commun 12:3976. https://doi.org/10.1038/s41467-021-24210-9

Ruan Y, Forsyth DW, Bell SW (2014) Marine sediment shear velocity structure from the ratio of displacement to pressure of Rayleigh waves at seafloor. J Geophys Res B Solid Earth 119:6357–6371. https://doi.org/10.1002/2014JB011162

Ruan Y, Forsyth DW, Bell SW (2018) Shear attenuation beneath the Juan de Fuca plate: Implications for mantle flow and dehydration. Earth Planet Sci Lett 496:189–197. https://doi.org/10.1016/j.epsl.2018.05.035

Sato H, Nakahara H, Ohtake M (1997) Synthesis of scattered energy density for nonspherical radiation from a point shear-dislocation source based on the radiative transfer theory. Phys Earth Planet Inter 104:1–13. https://doi.org/10.1016/S0031-9201(97)00050-2

Sato H, Fehler MC, Maeda T (2012) Seismic wave propagation and scattering in the heterogeneous earth, 2nd edn. Springer, Berlin Heidelberg, Berlin, Heidelberg

Shapiro NM, Campillo M, Singh SK, Pacheco J (1998) Seismic channel waves in the accretionary prism of the Middle America trench. Geophys Res Lett 25:101–104. https://doi.org/10.1029/97GL03492

Shinohara M, Hino R, Yoshizawa T et al (2005) Hypocenter distribution of plate boundary zone off Fukushima, Japan, derived from ocean bottom seismometer data. Earth, Planets and Space 57:93–105. https://doi.org/10.1186/BF03352553

Straume EO, Gaina C, Medvedev S et al (2019) GlobSed: updated total sediment thickness in the World's oceans. Geochem Geophys Geosyst 20:1756–1772. https://doi.org/10.1029/2018GC008115

Takagi R, Toyokuni G, Chikasada N (2020) Ambient noise correlation analysis of S-net records: extracting surface wave signals below instrument noise levels. Geophys J Int 224:1640–1657. https://doi.org/10.1093/gji/ggaa548

Takemoto T, Furumura T, Saito T et al (2012) Spatial- and frequency-dependent properties of site amplification factors in Japan derived by the coda normalization method. Bull Seismol Soc Am 102:1462–1476. https://doi.org/10.1785/0120110188

Takemura S, Furumura T, Maeda T (2015) Scattering of high-frequency seismic waves caused by irregular surface topography and small-scale velocity inhomogeneity. Geophys J Int 201:459–474. https://doi.org/10.1093/gji/ggv038

Takemura S, Kobayashi M, Yoshimoto K (2016) Prediction of maximum P- and S-wave amplitude distributions incorporating frequency- and distance-dependent characteristics of the observed apparent radiation patterns. Earth, Planets and Space 68:166. https://doi.org/10.1186/s40623-016-0544-8

Takemura S, Kobayashi M, Yoshimoto K (2017) High-frequency seismic wave propagation within the heterogeneous crust: effects of seismic scattering and intrinsic attenuation on ground motion modelling. Geophys J Int 210:1806–1822. https://doi.org/10.1093/gji/ggx269

Takemura S, Matsuzawa T, Kimura T et al (2018) Centroid moment tensor inversion of shallow very low frequency earthquakes off the Kii Peninsula, Japan, using a three-dimensional velocity structure model. Geophys Res Lett 45:6450–6458. https://doi.org/10.1029/2018GL078455

Takemura S, Kubo H, Tonegawa T et al (2019) Modeling of long-period ground motions in the Nankai subduction zone: model simulation using the accretionary prism derived from oceanfloor local s-wave velocity structures. Pure Appl Geophys 176:627–647. https://doi.org/10.1007/s00024-018-2013-8

Takemura S, Okuwaki R, Kubota T et al (2020a) Centroid moment tensor inversions of offshore earthquakes using a three-dimensional velocity structure model: slip distributions on the plate boundary along the Nankai trough. Geophys J Int 222:1109–1125. https://doi.org/10.1093/gji/ggaa238

Takemura S, Yabe S, Emoto K (2020b) Modelling high-frequency seismograms at ocean bottom seismometers: effects of heterogeneous structures on source parameter estimation for small offshore earthquakes and shallow low-frequency tremors. Geophys J Int 223:1708–1723. https://doi.org/10.1093/gji/ggaa404

Takemura S, Obara K, Shiomi K, Baba S (2022) Spatiotemporal variations of shallow very low frequency earthquake activity southeast off the Kii Peninsula, along the Nankai trough, Japan. J Geophys Res Solid Earth. https://doi.org/10.1029/2021JB023073

Todd EK, Schwartz SY, Mochizuki K et al (2018) Earthquakes and tremor linked to seamount subduction during shallow slow slip at the Hikurangi margin, New Zealand. J Geophys Res Solid Earth. https://doi.org/10.1029/2018JB016136

Tonegawa T, Araki E, Kimura T et al (2017) Sporadic low-velocity volumes spatially correlate with shallow very low frequency earthquake clusters. Nat Commun 8:2048. https://doi.org/10.1038/s41467-017-02276-8

Toomey D, Allen R, Barclay A et al (2014) The Cascadia initiative: a sea change in seismological studies of subduction zones. Oceanography 27:138–150. https://doi.org/10.5670/oceanog.2014.49

Trugman DT, Chu SX, Tsai VC (2021) Earthquake source complexity controls the frequency dependence of near-source radiation patterns. Geophys Res Lett. https://doi.org/10.1029/2021GL095022

Volk O, Shani-kadmiel S, Gvirtzman Z, Tsesarsky M (2017) 3D effects of sedimentary wedges and subsurface canyons: ground-motion amplification in the Israeli coastal plain. Bull Seismol Soc Am. https://doi.org/10.1785/0120160349

Wallace LM, Araki E, Saffer D et al (2016a) Near-field observations of an offshore Mw 6.0 earthquake from an integrated seafloor and subseafloor monitoring network at the Nankai trough, southwest Japan. J Geophys Res Solid Earth 121:8338–8351. https://doi.org/10.1002/2016JB013417

Wallace LM, Webb SC, Ito Y et al (2016b) Slow slip near the trench at the Hikurangi subduction zone New Zealand. Science 352:701–704. https://doi.org/10.1126/science.aaf2349

Wech AG (2021) Cataloging tectonic tremor energy radiation in the Cascadia subduction zone. J Geophys Res Solid Earth. https://doi.org/10.1029/2021JB022523

Wessel P, Smith WHF, Scharroo R et al (2013) Generic mapping tools: improved version released. Eos 94:409–410. https://doi.org/10.1002/2013EO450001

Wu W, Zhan Z, Peng S et al (2020) Seismic ocean thermometry. Science 369:1510–1515. https://doi.org/10.1126/science.abb9519

Yabe S, Tonegawa T, Nakano M (2019) Scaled energy estimation for shallow slow earthquakes. J Geophys Res Solid Earth 124:1507–1519. https://doi.org/10.1029/2018JB016815

Yabe S, Baba S, Tonegawa T et al (2021) Seismic energy radiation and along-strike heterogeneities of shallow tectonic tremors at the Nankai trough and Japan trench. Tectonophysics 800:228714. https://doi.org/10.1016/j.tecto.2020.228714

Yamashita Y, Yakiwara H, Asano Y et al (2015) Migrating tremor off southern Kyushu as evidence for slow slip of a shallow subduction interface. Science 348:676–679. https://doi.org/10.1126/science.aaa4242

Yamaya L, Mochizuki K, Akuhara T, Nishida K (2021) Sedimentary structure derived from multi-mode ambient noise tomography with dense OBS network at the Japan trench. J Geophys Res Solid Earth. https://doi.org/10.1029/2021JB021789

Yamaya L, Mochizuki K, Akuhara T et al (2022) CMT inversion for small-to-moderate earthquakes applying to dense short-period OBS array at off Ibaraki region. Earth Planets Space 74:164. https://doi.org/10.1186/s40623-022-01721-3

Yoshimoto K, Sato H, Ohtake M (1993) Frequency-dependent attenuation of P and S waves in the Kanto area, Japan, based on the coda-normalization method. Geophys J Int 114:165–174. https://doi.org/10.1111/j.1365-246X.1993.tb01476.x

Yoshimoto K, Takemura S, Kobayashi M (2015) Application of scattering theory to P-wave amplitude fluctuations in the crust. Earth Planets Space 67:199. https://doi.org/10.1186/s40623-015-0366-0

## Publisher's Note